ELSEVIER

Contents lists available at ScienceDirect

### Earth and Planetary Science Letters

www.elsevier.com/locate/epsl



## Evolving morphology of crustal accumulations in Earth's lowermost mantle



Mingming Li a,\*, Allen K. McNamara b

- <sup>a</sup> School of Earth and Space Exploration, Arizona State University, Tempe, AZ 85287-6004, USA
- <sup>b</sup> Department of Earth and Environmental Sciences, Michigan State University, East Lansing, MI 48824, USA

#### ARTICLE INFO

# Article history: Received 26 February 2021 Received in revised form 19 October 2021 Accepted 23 October 2021 Available online 4 November 2021 Editor: H. Thybo

Keywords: oceanic crust LLSVPs morphology lowermost mantle

#### ABSTRACT

Subducted oceanic crust is one of the major sources of compositional heterogeneity in Earth's mantle. It has been proposed that subducted oceanic crust may accumulate at the bottom of the Earth's mantle and cause the seismically-observed, Large Low Shear Velocity Provinces (LLSVPs). Testing this hypothesis requires a better understanding of the morphology of the crustal accumulations in the lowermost mantle. Here, through geodynamic modeling experiments, we find that thick subducted oceanic crust could accumulate into thermochemical piles with a height up to  $\sim 1000$  km above the core-mantle boundary (CMB), and the crustal accumulations typically have chemically fuzzy top boundaries and stratified interiors. As the oceanic crust thins with mantle cooling, it becomes more difficult to accumulate on the CMB, and the previous crustal accumulations gradually become smaller in size and gain sharp top boundaries and relatively homogeneous interiors. Our results suggest that if the present-day LLSVPs are mainly caused by the accumulations of subducted oceanic crust, they may be produced in the early hotter Earth when subducted oceanic crust may be thicker, and they may start with chemically fuzzy top boundaries and stratified interiors and gradually develop into chemically sharper top boundaries and more homogenized interiors.

© 2021 Elsevier B.V. All rights reserved.

#### 1. Introduction

Formed at mid-oceanic ridges by partial melting, the oceanic crust has different composition than the pyrolitic mantle in terms of both major and trace elements (Langmuir et al., 1992). Oceanic crust is subducted to the deep mantle at subduction zones and becomes one of the major sources of the compositional heterogeneity in the Earth's deep mantle. After transformed into eclogite, subducted oceanic crust becomes intrinsically denser than the pyrolitic mantle at most mantle depths except in the uppermost lower mantle (e.g., Hirose et al., 2005; Kesson et al., 1994; Ringwood and Irifune, 1988). Recent high-temperature-pressure experiments by (Ko et al., 2020) showed that, despite its higher MgO content, Archean oceanic crust at depths >~800 km depth has a similar (or slight lower) positive intrinsic density anomaly with respect to pyrolite than the intrinsic density anomaly of modern oceanic crust. Due to its increased intrinsic density, a significant amount of subducted oceanic crust may accumulate at the bottom of the mantle (e.g., Brandenburg et al., 2008; Brandenburg and van Keken, 2007; Christensen and Hofmann, 1994; Davies, 2008; Mulyukova et al., 2015; Nakagawa and Tackley, 2005; Nakagawa and Tackley, 2010, 2014, 2015; Nakagawa et al., 2010; Ogawa, 2003).

Seismic observations have revealed two large-low shear velocity provinces (LLSVPs) in the lowermost mantle, one beneath Africa and the other beneath Pacific Oceans (see a review paper by Garnero et al., 2016 for more information). The LLSVPs are among the largest structures in the lowermost mantle, which may greatly affect the CMB heat flux (Li et al., 2018; Nakagawa and Tackley, 2005; Nakagawa and Tackley, 2010, 2014), the formation of mantle plumes and surface intraplate volcanism (e.g., Li and Zhong, 2017; Torsvik et al., 2010), and perhaps the surface plate motion as well (Trim et al., 2014). One hypothesis is that the LLSVPs are caused by accumulations of subducted oceanic crust (e.g., Christensen and Hofmann, 1994; Garnero et al., 2016; Jones et al., 2020; Thomson et al., 2019). This hypothesis provides a key to understand both the origin of the largest seismic structures in Earth's mantle and the dynamics and evolution of the subducted oceanic crust.

However, verification of the hypothesis that the LLSVPs are caused by subducted oceanic crust remains challenging. Mineral physics experiments and theoretical analyses have been conducted to measure or estimate the seismic velocities of oceanic crust under lowermost mantle conditions, but the results are controversial: whereas (Deschamps et al., 2012) and (Wang et al., 2020) con-

<sup>\*</sup> Corresponding author.

E-mail address: Mingming.Li@asu.edu (M. Li).

cluded that the seismic velocities of LLSVPs cannot be explained by subducted oceanic crust, (Thomson et al., 2019) and (Jones et al., 2020) reached the opposite conclusion. If the LLSVPs are caused by subducted oceanic crust, they may be intrinsically denser than the surrounding mantle. However, the density of the LLSVPs remains a matter of debate (e.g., Koelemeijer et al., 2017; Lau et al., 2017) and separating the chemical and thermal effects on the density of LLSVPs is also challenging (e.g., Deschamps et al., 2012). Geochemical observations have suggested that the source of Ocean-island basalts (OIBs) often contains recycled oceanic crust (e.g., Cabral et al., 2013; Sobolev et al., 2011), together with other compositional components such as primitive materials and depleted mantle materials (e.g., Hofmann, 1997). The OIBs are often interpreted as caused by mantle plumes which have been suggested to preferentially origin from the margins of LLSVPs (e.g., Li and Zhong, 2017; Torsvik et al., 2010). Therefore, the hypothetical crustal origin of LLSVPs seems to be consistent with geochemical observations. However, mantle plumes may also sample subducted oceanic crust from outside the LLSVPs (Li, 2021; Li et al., 2014a) and the observation of recycled oceanic crust in OIB sources is not sufficient to conclude that the LLSVPs are caused by subducted oceanic crust.

This study examines the morphology of the accumulations of subducted oceanic crust in the lowermost mantle, which helps understand the observed features of the LLSVPs and test whether the LLSVPs are caused by subducted oceanic crust. It has been found that the ability for the subducted oceanic crust to accumulate on the CMB strongly depends on the thickness of the subducted oceanic crust, with a thicker subducted oceanic crust more likely to accumulate on the CMB than a thinner one (e.g., Christensen and Hofmann, 1994; Davies, 2008; Li and McNamara, 2013). In addition, the crustal accumulations often exhibit a chemically fuzzy top boundary where crustal materials are typically mixed with a large amount of intrinsically less dense background mantle materials (e.g., Brandenburg et al., 2008; Brandenburg and van Keken, 2007; Christensen and Hofmann, 1994; Davies, 2008; Mulyukova et al., 2015; Nakagawa and Tackley, 2005; Nakagawa and Tackley, 2010, 2014, 2015; Nakagawa et al., 2010; Ogawa, 2003). However, melt production rate at mid-ocean ridge is significantly controlled by uppermost mantle temperature (e.g., Langmuir et al., 1992; Li et al., 2016; McKenzie and Bickle, 1988), and the oceanic crust may be much thicker in the past when the mantle was hotter (e.g., McKenzie and Bickle, 1988). It remains unclear how the morphology of crustal accumulations evolves with the cooling of Earth's mantle. Here, we perform geodynamic modeling experiments to investigate this problem.

#### 2. Methods

The following non-dimensional conservation equations are solved under the Boussinesq approximation using the finite element CitcomCU code (Zhong, 2006):

$$\nabla \cdot \overrightarrow{u} = 0, \tag{1}$$

$$-\nabla P + \nabla \cdot (\eta \dot{\epsilon}) = \xi^{-3} \left[ Ra \left( T - \sum_{i} B_{i} C_{i} \right) + Ra_{p} \Gamma \right] \hat{r}, \tag{2}$$

$$\frac{\partial T}{\partial t} + (\overrightarrow{u} \cdot \nabla)T = \nabla^2 T + Q, \tag{3}$$

where,  $\overrightarrow{u}$  is the velocity, P is the dynamic pressure,  $\eta$  is the viscosity,  $\dot{\epsilon}$  is the strain rate, Ra is the Rayleigh number, T is the temperature,  $B_i$  and  $C_i$  are the buoyancy number and the fraction of the ith composition, respectively;  $Ra_p$  and  $\Gamma$  are the phase transition Rayleigh number and the phase function, respectively;  $\hat{r}$ 

**Table 1** Definition of symbols and their values.

Parameters	Symbol	Value
Earth's radius	R <sub>e</sub>	6371 km
Mantle thickness	D	2890 km
Reference density	$ ho_0$	$3300 \text{ kg/m}^3$
Thermal expansivity	α	$1 \times 10^{-5} \text{ K}^{-1}$
Thermal diffusivity	κ	$1 \times 10^{-6} \text{ m}^2/\text{s}$
Gravitational acceleration	g	9.8 m/s <sup>2</sup>
Reference temperature	$\Delta T$	3000 K
Reference viscosity	$\eta_0$	
Non-dimensional temperature	T	
Non-dimensional internal heating rate	Q	
Thickness of oceanic crust	$H_c$	
Buoyancy number of oceanic crust	$B_{c}$	
Thickness of depleted lithosphere	$H_l$	
Buoyancy number of depleted lithosphere	$B_l$	
Effective buoyancy ratio of an element	B <sup>eff</sup>	
Background mantle temperature at 300 km	$T_{300}$	
Transit time	t*	
Areal fraction of the model domain that is occupied by PCA elements	Fa	
The ratio of crustal content in PCA elements relative to the total crustal content	$R_n$	
The average effective buoyancy ratio from all PCA elements	$\overline{B}_{pca}$	
The standard deviation of effective buoyancy ratio from all PCA elements	$\overline{B}_{pca}^{std}$	
The average age of crustal tracers within PCA elements	$\overline{A}_{pca}$	

is the unit vector in radial direction, t is the time, Q is the internal heat generation rate, and  $\xi = D/R_e$ , with D the thickness of Earth's mantle and  $R_e$  the Earth's radius.

The Rayleigh number is defined as:

$$Ra = \frac{\rho_0 g \alpha \Delta T D^3}{\eta_0 \kappa},\tag{4}$$

where  $\rho_0$ , g,  $\alpha$ ,  $\Delta T$ ,  $\eta_0$  and  $\kappa$  are, respectively, the reference density (which is the intrinsic density of the background mantle in this study), the gravitational acceleration, the thermal expansivity, the reference temperature (which is the temperature difference between CMB and surface in this study), the reference viscosity at temperature, and the thermal diffusivity. The symbols and values of physical parameters used in this study are provided in Table 1.

The phase transition Rayleigh number is defined as:

$$Ra_p = \frac{\Delta \rho_p}{\rho_0 \alpha \Delta T} Ra,\tag{5}$$

where  $\Delta \rho_p$  is the density change of the phase transition.

The whole mantle dynamics is modeled in a 2D spherical annulus geometry (Hernlund and Tackley, 2008), and the model setup is similar to our previous work (Li and McNamara, 2018). The model domain is divided into 3840 and 256 elements in lateral and radial direction, respectively. The grid is gradually refined in the radial direction towards the top and the bottom, resulting in 3 km and 6 km resolution on the top 6 km and bottom 600 km, respectively. Both the top surface and the CMB are free-slip. The models are both internally and basally heated, with an internal heating rate of Q = 60 for most cases that lead to an internal heating ratio of 50–80%. Isothermal temperature boundary conditions are applied at the surface (T = 0) and the CMB (T = 1).

We employed a Rayleigh number of  $Ra=5\times 10^7$  for most cases. The viscosity is given by  $\eta=\eta_r\exp[A(0.6-T)]$ , where A is the activation coefficient and we use A=9.21 for most cases, which allows a maximum viscosity contrast of  $10^4$  due to changes of temperature, and  $\eta_r$  is 1.0 in the upper mantle (from 0–660 km depth) and 50.0 in the lower mantle (from 660 km to the CMB). Mineral physics studies have suggested that the Bridgmanite to post-Perovskite (pPv) phase transition may lead to 10–1000 times viscosity reduction (Ammann et al., 2010; Hunt et al., 2009). We include this phase transition in some models. The phase function for the pPv phase transition is defined as:

$$\Gamma(\pi) = 0.5 + 0.5 \tanh\left(\frac{\pi}{w}\right),\tag{6}$$

where w = 0.0047 (or 30 km) is the dimensionless width of the phase transition and  $\pi$  is the excess pressure which is defined as:

$$\pi = d - d_{ppv} - \gamma (T - T_{ppv}), \tag{7}$$

where d is depth, T is temperature,  $\gamma=0.1747$  (with a dimensional value of 12 MPa/K) is the Clayperon slope, and  $d_{ppv}=0.4328$  (or 2700 km when scaled with the radius of the Earth) is the depth for the phase transition at temperature of  $T_{ppv}=0.473$  (which is equivalent to a dimensional temperature of  $\sim 2640$  K when scaled with a reference temperature of  $\Delta T=3000$  K and adding back the adiabatic temperature increase at 2700 km depth with a gradient of 0.35 K/km and surface temperature of 273 K).

Our models contain three different compositional components: background mantle material, oceanic crust, and depleted lithosphere material. The composition field is simulated using the ratio tracer method (Tackley and King, 2003) with  $\sim$ 40 million tracers (e.g.,  $\sim$ 40 tracers per element on average). Initially, the entire computational domain is randomly filled with tracers that represent the background mantle material. When tracers are advected upwards and cross the bottoms of the oceanic crust or the depleted lithosphere, they are changed into crustal or depleted lithospheric type of tracers, respectively. The depleted lithosphere is kept at 9 times thicker than the oceanic crust, assuming an average of 10% partial melting (e.g., Langmuir et al., 1992). The buoyancy numbers for the oceanic crust ( $B_c$ ) and the depleted lithosphere material ( $B_l$ ) are defined as:

$$B_c = \frac{\Delta \rho_c}{\rho_0 \alpha \Delta T},\tag{8}$$

$$B_l = \frac{\Delta \rho_l}{\rho_0 \alpha \Delta T},\tag{9}$$

where  $\Delta \rho_c$  and  $\Delta \rho_l$  are, respectively, the intrinsic density anomalies of the oceanic crust and the depleted lithosphere material with respect to the background mantle material. We use a buoyancy number of  $B_c = 0.8$  for most cases, which is equivalent to a  $\sim 2.4\%$  intrinsic density anomaly that is about in the middle of the range of  $\sim 1-5\%$  at most mantle depths as constrained in mineral physical experiments (e.g., Hirose et al., 2005; Kesson et al., 1994; Ko et al., 2020; Ringwood and Irifune, 1988), but cases with a different  $B_c$  are also performed. The buoyancy number of the depleted lithosphere is set to be related to that of the oceanic crust by  $B_l = 0.0 - B_c/9.0$ . Like (Li et al., 2017), the effective intrinsic density anomaly of each element is calculated by averaging the densities of each component, leading to an effective buoyancy ratio:

$$B^{eff} = \frac{\sum_{i} (\Delta \rho_{i} * C_{i})}{\rho \alpha \Delta \rho},$$
(10)

where  $C_i$  is the fraction of the *i*th compositional component in the element

The main goal of this study is to test how the morphology of accumulations of subducted oceanic crust evolves with the cooling of mantle (and the resulted thinning of oceanic crust). Therefore, our models start with a relatively hot mantle that generally cools with time. To obtain a proper temperature initial condition, we first perform a lower resolution (with  $1280 \times 128$  elements) isochemical calculation with an initial temperature of T = 0.72everywhere. We calculate the average background mantle temperature at 300 km,  $T_{300}$ , by averaging the temperature in all regions at this depth excluding the relatively cold regions with  $T < T_{ave}$ , where  $T_{ave}$  is the horizontally averaged temperature (similar to Zhong, 2006 and Li et al., 2018). After the  $T_{300}$  of this lower resolution model decreases to  $T \sim 0.62$  (or  $\sim 1860$  K when scaled by  $\Delta T = 3000$  K), the temperature field is interpolated to higher resolution (3840  $\times$  256 elements) and is used as the initial temperature condition for cases presented in this study.

The thickness of oceanic crust generated at the surface,  $H_c$ , is related to  $T_{300}$  by

$$H_c = 6.0 + 340 \times (T_{300} - 0.52),$$
 (11)

which leads to a linear decrease of  $H_C$  from 40 km for  $T_{300} = 0.62$ or 1860 K to 6 km for  $T_{300} = 0.52$  or 1560 K, consistent with the estimations of (McKenzie and Bickle, 1988). Similar equation as Eq. (11) has been used to calculate the thickness of oceanic crust generated by fertile (undepleted) mantle as a function of upper mantle temperature by (Davies, 2008). However, the actual thickness of oceanic crust used in the models of (Davies, 2008) is  $\sim$ 3-6 km and does not decrease with mantle cooling. This thin crust is caused by that the production of oceanic crust in (Davies, 2008) is simulated by moving crustal tracers from a melting zone in the uppermost mantle to a thin crustal layer, but the upper mantle in the models of (Davies, 2008) is often depleted of crustal tracers. In contrast with (Davies, 2008), we assume that the thickness of oceanic crust is to the first order controlled by uppermost mantle temperature, and do not consider the effects of chemical heterogeneities which are not well understood (e.g., Langmuir et al., 1992). For comparison, two models with a fixed thickness of oceanic crust are performed. It should also be pointed out that our models do not generate self-consistent sustainable Earth-like asymmetric plate subduction which is a grand challenge in geodynamic modeling experiments. In our models, the oceanic crust produced at the surface is first advected to convergent regions of the uppermost mantle where it forms small crustal accumulations from which a portion of crustal materials are advected to the deep mantle (e.g., Fig. 1). This mechanism of subducting oceanic crust to the deep mantle is greatly controlled by the lithosphere viscosity which depends on temperature. Because the lithosphere temperature does not change with time due to the fixed temperature boundary condition on the top surface, the time evolution of the thickness of subducted oceanic crust in the deep mantle is to the first order determined by that of the oceanic crust generated at the surface.

Another consequence of not capturing Earth-like subduction in our models is that the surface velocity is relatively small ( $\sim\!0.7$  cm/yr for cases with Ra =  $5\times10^7$  and  $\sim\!0.3$  cm/yr for cases with Ra =  $1\times10^7$ ). As a result, the time it takes for an oceanic crust to sink from surface to deep mantle is much longer than that for the real Earth that has a present-day average plate velocity of  $\sim\!5$  cm/yr. To better scale with the real Earth, we follow previous studies (e.g., Christensen and Hofmann, 1994; Li and McNamara, 2013, 2018) and present the elapsed time of dynamic processes in terms of transit time,  $t^*$ , which is defined as:

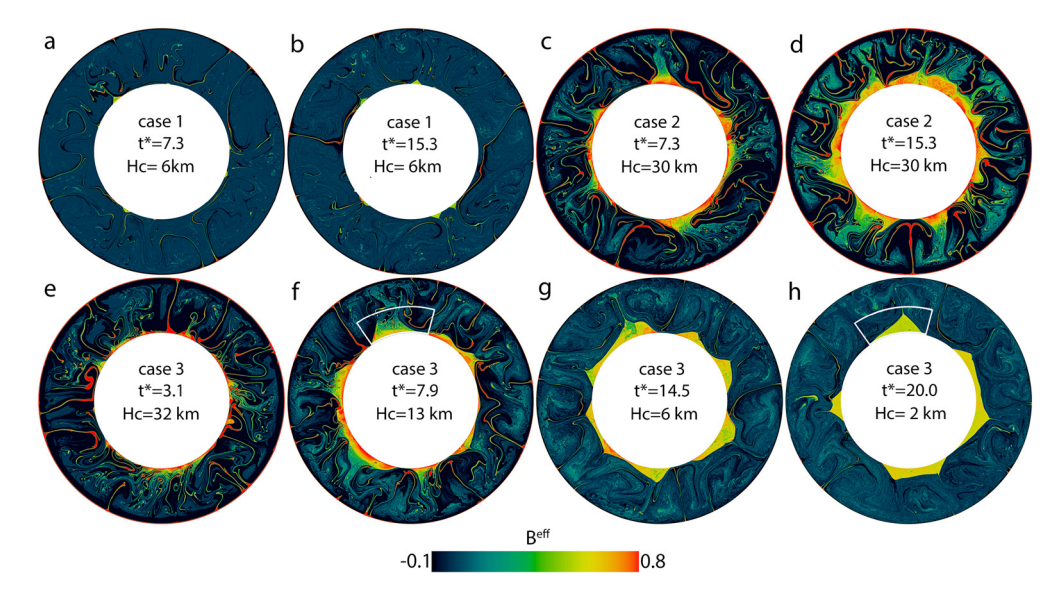


**Fig. 1.** Snapshots of compositional fields (represented by the effective buoyancy ratio) for case 1 (**a, b**), case 2 (**c, d**) and case 3 (**e-h**).  $H_c$  and  $t^*$  in each panel are the thickness of oceanic crust and the transit time, respectively.

$$t^* = \frac{1}{\xi} \int_0^t \overline{u}(t')dt', \tag{12}$$

where t is the non-dimensional time,  $\overline{u}(t')$  is the average surface velocity at non-dimensional time t', and  $\xi$  is defined previously in equation (2). One transit time is defined as the time a slab takes to sink from the surface to the CMB. To relate transit time to geological timescale, previous studies often assume that 1 transit time is equivalent to 60 Myr (e.g., Christensen and Hofmann, 1994; Li and McNamara, 2013). All cases are run for more than 20 transit times. For reference, the dimensional time calculated using a diffusion time scale (by multiplying the non-dimensional time with  $R_e^2/\kappa$ ) is plotted against the transit time in Supplementary Information Figure S1.

#### 3. Results

Table 2 lists the parameters for all cases used in this study. We first show the results of cases 1–2 with constant thickness of oceanic crust. In case 1, the oceanic crust has a constant thickness of 6 km and a buoyancy number of  $B_{\rm c}=0.8$  (or  $\sim$ 2.4% denser than the background mantle materials). After the subducted oceanic crust reaches the lowermost mantle, most of it is viscously entrained up and stirred into the background mantle (Figs. 1a-b). We find that it is difficult for a thin oceanic crust to accumulate on the CMB, which confirms the conclusions in our previous studies (Li and McNamara, 2013) in which models were performed in 2D Cartesian geometry.

Case 2 has the same parameters as Case 1, except that the oceanic crust has a constant thickness of 30 km. Compared to case 1, the subducted oceanic crust is thicker and easier to accumulate on the CMB, and it makes large piles of crustal accumulations (hereinafter referred to as PCAs) in the lowermost mantle. The PCAs are characterized by chemically fuzzy top boundaries where the crustal material is mixed with a large amount of other intrinsically less dense materials (e.g., depleted lithosphere material and background mantle material). The concentration of crustal material within the PCAs also generally increases with depth (e.g., higher crustal concentration leads to larger effective buoyancy ratio) (Figs. 1c-d).

In case 3, the thickness of oceanic crust generated at the surface deceases with uppermost mantle temperature according to

**Table 2**Cases used in this study and their parameters.

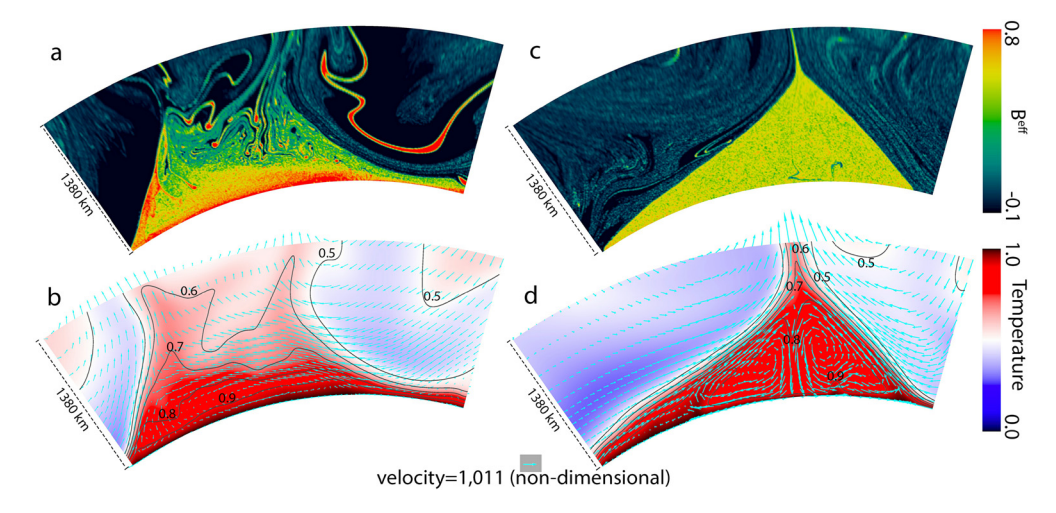
Case	Ra	Α	Q	$B_c$	H <sub>c</sub>	weak pPv
1	5e7	9.21	60	0.8	6 km	no
2	5e7	9.21	60	0.8	30 km	no
3	5e7	9.21	60	0.8	T-dependent	no
4	5e7	9.21	60	0.6	T-dependent	no
5	5e7	4.91*	60	0.8	T-dependent	no
6	5e7	9.21	60	0.8	T-dependent	yes
7	1e7	9.21	30	0.8	T-dependent	no

Ra: Rayleigh number; A: activation parameter for temperature-dependent viscosity; Q: internal heating rate;  $B_c$ : buoyancy number for oceanic crust;  $H_c$ : thickness of oceanic crust. The thickness of oceanic crust for cases 3–7 is temperature dependent following Eq. (11). \*: A = 4.91 in the lower mantle and 9.21 in the upper mantle for case 5

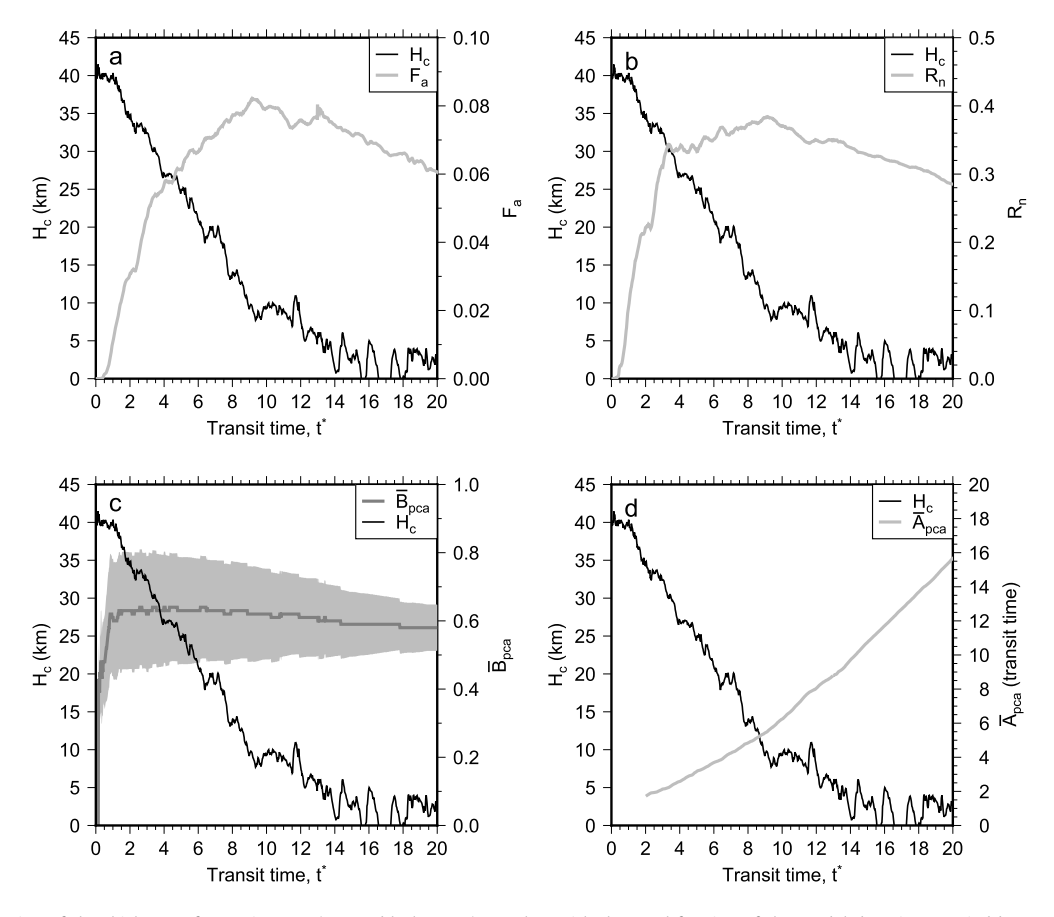
Eq. (11), whereas other parameters are the same as cases 1–2. Figs. 1e-h shows a time series of snapshots for the composition field of case 3. Large PCAs form on the CMB at early times when the subducted oceanic crust is thick, with chemically fuzzy top boundaries (Figs. 1e-f). The intrinsic density anomaly (as represented by  $B^{\rm eff}$ ) of the PCAs also generally increases with depth (Figs. 1e-f). However, as the oceanic crust becomes thinner, the top boundaries of the PCAs gradually become sharper. The internal density anomaly of the PCAs also gradually become more homogeneous (Figs. 1g-h).

Fig. 2 shows the zoomed-in views of the composition and temperature fields of a PCA for case 3 at  $t^*=7.9$  (Figs. 2a-b) and  $t^*=20.0$  (Figs. 2c-d). The PCA reaches a height of  $\sim$ 1000 km above the CMB. At  $t^*=7.9$ , the top boundary of the PCA is chemically fuzzy, with materials being advected across the tops of the PCA (Fig. 2a). The PCA also has a layered internal structure with the intrinsic density anomaly generally increasing with depth (Fig. 2a) and its upper portion much cooler than the lower portion (Fig. 2b). At  $t^*=20.0$ , the PCA has sharp boundaries (Fig. 2c) where the component of the mantle flow velocities normal to the PCA's margins almost vanishes (Fig. 2d), and only a thin trace of crustal materials is entrained out from the top of the PCA (Fig. 2c). Circular convection pattern develops within the PCA (Fig. 2d) and the intrinsic density anomaly and the temperature of the PCA become much more homogeneous (Figs. 2c-d).

To further quantify the results, we define each element of the model domain as a PCA element if it has an average temperature



**Fig. 2.** The composition field  $(\mathbf{a}, \mathbf{c})$  and the temperature field  $(\mathbf{b}, \mathbf{d})$  zoomed-in at regions outlined by the white boxes in Fig. 1f at  $t^* = 7.9$   $(\mathbf{a}, \mathbf{b})$  and Fig. 1h at  $t^* = 2.0.0$   $(\mathbf{c}, \mathbf{d})$  for case 3. The composition field is represented by the effective buoyancy ratio. The black contours the temperature field show temperature isotherms at 0.9, 0.8, 0.7, 0.6 and 0.5.



**Fig. 3.** The time evolution of the thickness of oceanic crust (or  $H_c$ , black curve) together with the areal fraction of the model domain occupied by PCAs, or  $F_a$  (a), the ratio of the number of crustal tracers in PCAs relative to the total number of crustal tracers in the model domain, or  $R_n$  (b), the average effective buoyancy ratio in PCA elements, or  $\overline{B}_{pca}$ , and the standard deviation, or  $\overline{B}_{pca}^{std}$  (c), and the average age crustal tracers in PCAs, or  $\overline{A}_{pca}$  (d), for case 3.  $\overline{A}_{pca}$  is only shown at  $t^* > 2.0$  when the area of PCAs is significant (shown in panel a).

T>0.5 and an effective buoyancy ratio  $B^{eff}>0.3$  (e.g., containing a significant concentration of subducted oceanic crust). We calculate the time evolution of (1) the areal fraction of the model domain that is occupied by PCA elements, or  $F_a$  (Fig. 3a), (2) the ratio between the number of crustal tracers in PCA elements and the total number of crustal tracers in the model domain, or  $R_n$  (Fig. 3b), and (3) the average of the effective buoyancy ratio from all PCA elements, or  $\overline{B}_{pca}$ , and the standard deviation,  $\overline{B}_{pca}^{std}$  (Fig. 3c).

The age of each crustal tracer at each timestep is computed using the elapsed time at this timestep minus the time when the crustal tracer is initially changed from other types of tracers and introduced to the model domain. The average age of crustal tracers within PCA elements is calculated, which is denoted as  $\overline{A}_{pca}$  (Fig. 3d). For convenience, we refer the accumulation rate to the rate by which subducted oceanic crust accumulates into PCAs, and we refer the entrainment rate to that by which materials from the

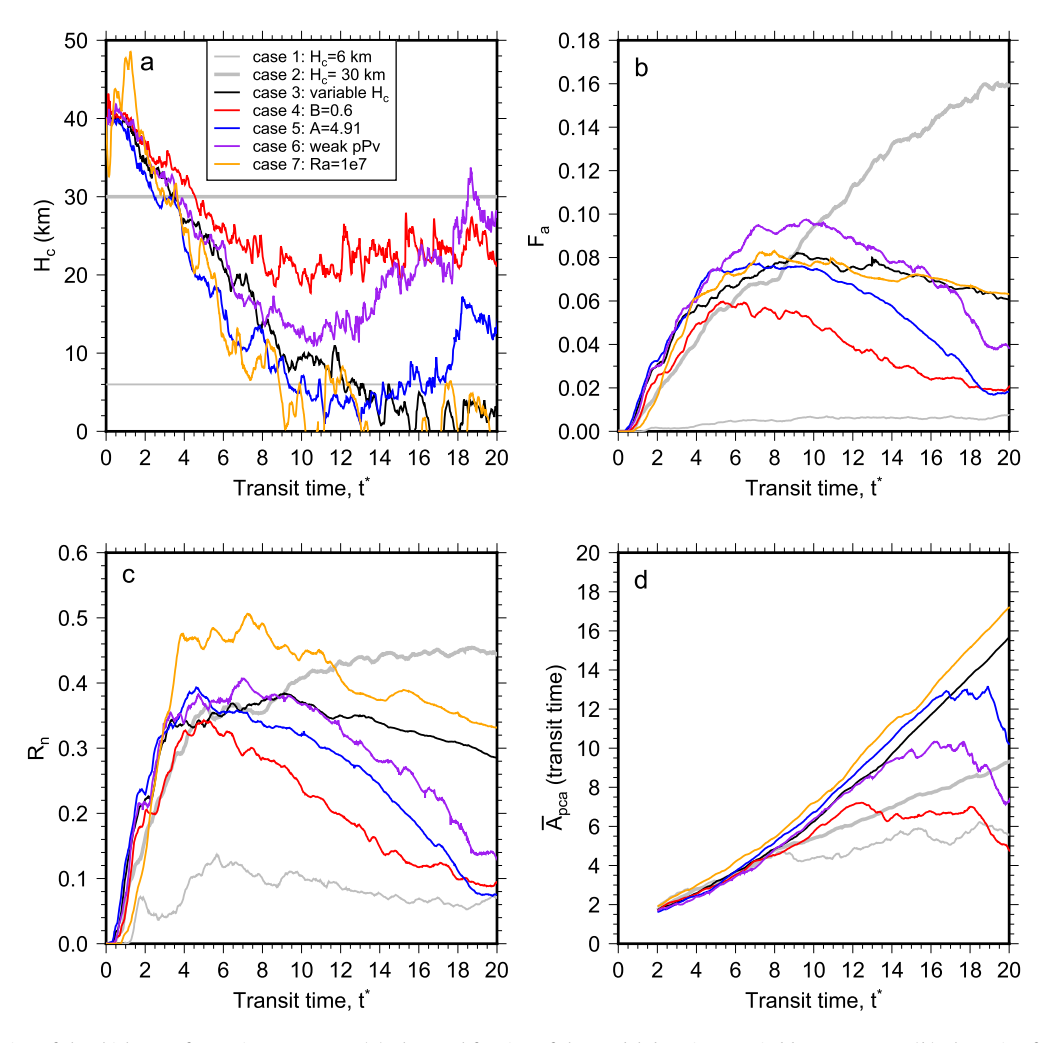


**Fig. 4.** The time evolution of the thickness of oceanic crust, or  $H_c$  (a), the areal fraction of the model domain occupied by PCAs, or  $F_a$  (b), the ratio of the number of crustal tracers in PCAs relative to the total number of crustal tracers in the model domain, or  $R_n$  (c), and the average age of PCAs, or  $\overline{A}_{pca}$  (d), for cases 1–7.

PCAs are entrained and stirred into the background mantle. We summarize the symbols used in this study in Table 1.

As shown in Fig. 3a,  $F_A$  in case 3 first increases with time when the oceanic crust is thicker than  $\sim 10$  km before  $t^* \sim 9.0$ . After that,  $F_A$  decreases with time while the oceanic crust thins, indicating that the entrainment rate is higher than the accumulation rate. The time evolution of  $R_n$  closely follows that of  $F_a$ , which first increases to a maximum value of  $\sim 0.4$  at  $t^* \sim 9.0$  and then decreases linearly to  $\sim 0.3$  at  $t^* = 20.0$  (Fig. 3b).

As shown in Fig. 3c,  $\overline{B}_{pca}$  is 0.0 at  $t^* = 0.0$  because initially there is no subducted oceanic crust in the mantle. Shortly after the initial condition,  $\overline{B}_{pca}$  quickly reaches a maximum value of  $\sim$ 0.6. The smaller value of  $\overline{B}_{pca}$  than  $B_c = 0.8$  is because the intrinsically less dense background mantle materials and depleted lithospheric materials are stirred into the PCAs. This stirring process occurs throughout the model run, and because of it,  $\overline{B}_{pca}$ generally decreases with time. The standard deviation of the average effective buoyancy ratio within PCA elements, or  $\overline{B}_{pca}^{std}$ , also gradually decreases with time (gray regions in Fig. 3c), indicating that the compositional components (background mantle, oceanic crust, and depleted lithosphere) within the PCAs are more evenly mixed as time goes by. The increasing degree of mixing with time is in accordant with the development of internal convection within the PCAs (e.g., Fig. 2d). As shown in Fig. 3d,  $\overline{A}_{pca}$  in case 3 increases with time with a higher rate at later stages of the calculation than at earlier stages, indicating that newly formed oceanic crust is more difficult to accumulate into PCAs at the later stages.

We perform additional cases to investigate how the morphology of PCAs is affected by the intrinsic density of oceanic crust, the degree of temperature dependence of viscosity, the presence of weak pPv phase in the lowermost mantle, and the vigor of mantle convection (Table 2). Fig. 4 compares the time evolution of  $H_c$ (Fig. 4a),  $F_a$  (Fig. 4b),  $R_n$  (Fig. 4c), and  $\overline{A}_{pca}$  (Fig. 4d) for all cases. Compared to case 3, case 4 has a lower buoyancy number of the oceanic crust of  $B_c = 0.6$  (or  $\sim 1.8\%$  denser than the background mantle materials). The results of case 4 are shown by the red curves in Fig. 4. In case 4,  $H_c$  generally decreases with time to  $\sim 20$ km at  $t^* \sim 10.0$  and then remains relatively stable.  $F_a$  and  $R_n$  first increase to maximum values at  $t^* \sim 5.0$  and then decreases with time. Although the oceanic crust is thicker than case 3, the reduced buoyancy number makes the subducted oceanic crust more difficult to accumulate into PCAs and more importantly, makes the PCAs less stable and easier to be stirred into the background mantle. As a result, both  $F_a$  and  $R_n$  are smaller than case 3. The time evolution of  $\overline{A}_{pca}$  first follows similar trend as that in case 3 until  $t^* \sim 12.0$ , then  $\overline{A}_{pcq}$  become much smaller than case 3.

In case 5, the activation coefficient for the temperature-dependent viscosity is reduced to A=4.91 in the lower mantle but is kept the same as case 3 in the upper mantle to obtain similar viscosity in the lithosphere and surface mobility as case 3. The results of case 5 are shown by the blue curves in Fig. 4. In case 5, the  $H_c$  first deceases with similar rate as case 3 until  $t^*\sim16.0$  after which it increases with time. The increase of  $H_c$  at later stages of the calculation is because as the PCA area decreases, their ther-

mal insulation effects on the core are less significant, which results in increases of CMB heat flux and mantle temperature (e.g., Li and McNamara, 2018). However, the thickening of the oceanic crust at the late stages of the calculation does not lead to more crustal accumulations: whereas  $F_a$  and  $R_n$  reach similar peak values than case 3 at  $t^* \sim 4.0$ , they decrease with a much higher speed afterward than that in case 3. Like case 4,  $\overline{A}_{pca}$  in case 5 first increases with time with similar rate as in case 3 until  $t^* \sim 16.0$  after which it becomes relatively stable for  $\sim 2$  transit times and then quickly decreases with time.

In case 6, we employ a  $500\times$  reduction of viscosity and 1% density increase due to the pPv phase transition. The results of case 6 are shown by the purple curves in Fig. 4. In case 6,  $H_c$  first decreases with time until  $t^*\sim 12.0$  then increases with time.  $F_a$  and  $R_n$  reach higher maximum values than case 3 at  $t^*\sim 7.0$ –10.0, and then decrease with higher rates than case 3. Like case 4 and case 5,  $\overline{A}_{pca}$  in case 6 first increases with the same rate as case 3 until  $t^*\sim 13.0$  after which the rate of increase is significantly reduced and eventually becomes negative (e.g., the PCAs are getting younger). The reduction of the rate of increase for  $\overline{A}_{pca}$  in cases 4–6 during the late stages of the model run are likely caused by the rapid entrainment of materials from old PCAs to the background mantle and, to a less extent, the addition of relatively younger subducted oceanic crust to the PCAs.

In case 7, we use a  $5\times$  lower Rayleigh number than case 3. We also employ a lower internal heating rate of Q=30 to obtain a similar upper mantle temperature as in case 3, because the mantle temperature is inversely proportional to Rayleigh number in models with internal heating (O'Farrell and Lowman, 2010). The results of case 7 are shown by the orange curves in Fig. 4. The time evolution of  $H_c$  in case 7 is similar to that in case 3. Compared to case 3, less amount of oceanic crust is generated in case 7 (Supplementary Information Figure S2). However, because case 7 has higher  $R_n$  (or rate of crustal segregation), its  $F_a$  (or area of PCAs) is similar to case 3. Case 7 also has slightly larger  $\overline{A}_{pca}$  (e.g., older PCAs) than case 3.

For comparison, Fig. 4 also shows  $F_a$ ,  $R_n$  and  $\overline{A}_{pca}$  for case 1 (thin gray curves) and case 2 (thick gray curves) that have constant  $H_c$  of 6 km and 30 km, respectively. In case 1,  $F_a$  continuously increases to only  $\sim 0.01$  after 20.0 transit times, and it is much smaller than other cases.  $R_n$  in case 1 is also much smaller than other cases except near the end of the model run when  $R_n$  in cases 4 and 5 decreases to similar values as case 1.  $\overline{A}_{pca}$  in case 1 is much smaller than other cases, indicating that the PCAs in case 1 are continuously refreshed. In case 2, both  $F_a$  and  $R_n$  keep increasing with time and reach much higher values at  $t^* = 20.0$ than other cases. The PCAs in case 5 are younger than that in case 3 because newly formed crustal materials are continually added to the PCAs in case 5. An interesting finding is that whereas the total number of crustal tracers first increases quickly with time and then becomes stable for cases 3-7 in which the crustal thickness generally decreases with time, the total number of crustal tracers in cases 1-2 (with constant crustal thickness) keeps increasing with time throughout the model run (Supplementary Information

Like Figs. 1e-h for case 3, Fig. 5 shows snapshots of the compositional fields for cases 4–7. One common feature in cases 3–7 is that large PCAs form when the oceanic crust is thick, and they show chemically fuzzy top boundaries and layered internal structures. As the oceanic crust becomes thinner, it is also more difficult to accumulate on the CMB. In addition, the PCAs gradually gain sharp boundaries and more homogeneous interiors. At early stages of the calculations, the accumulations of subducted oceanic crust often form connected, stratified layers on the CMB. As time goes by, they are pushed by mantle convection into spatially isolated thermochemical piles. The change in morphology and inter-

nal structures of the PCAs occurs gradually, and some PCAs develop sharp boundaries sooner than others (e.g., Fig. 5e). Even a single isolated PCA can have chemically sharp top boundaries in some parts and fuzzy top boundaries in other parts (e.g., Fig. 5h).

#### 4. Discussion

Here, we show that a thick subducted oceanic crust in the early hotter mantle could accumulate into large piles of crustal accumulations, or PCAs, in the lowermost mantle with chemically fuzzy top boundaries and stratified interiors, and the size of PCAs generally increases with time to a height up to  $\sim$ 1000 km above the CMB. These phenomena have been observed in previous geodynamic modeling studies as well (e.g., Brandenburg et al., 2008; Christensen and Hofmann, 1994; Davies, 2008; Mulyukova et al., 2015; Nakagawa and Tackley, 2005; Nakagawa and Tackley, 2010, 2014, 2015; Nakagawa et al., 2010; Ogawa, 2003). A new finding of this study is that as mantle cools and oceanic crust becomes thinner, the subducted oceanic crust is more difficult to accumulate in the lowermost mantle. In addition, the previous formed PCAs gradually develop into sharp top boundaries and relatively more homogeneous interiors, and the size of PCAs typically decreases with time due to the entrainment of materials from PCAs to the background mantle.

We find that the morphology of PCAs and its speed of evolution are significantly controlled by the thickness and the intrinsic density anomaly of subducted oceanic crust, the lowermost mantle viscosity, and the vigor of convection. As shown in Fig. 4c, whereas ratio of crustal content in PCA elements relative to the total crustal content,  $R_n$ , increases from 0.0 to similar peak values of  $\sim$ 0.34-0.39 after  $\sim$ 4-5 transit times in cases 4-6 and case 3, it decreases to  $\sim$ 0.09,  $\sim$ 0.08 and  $\sim$ 0.14 at 20.0 transit times for cases 4, 5, and 6, respectively, which is much lower than that in case 3 which is  $\sim$ 0.29. These results indicate that cases 4-6 have similar accumulation rate than case 3 during the early stages of the calculations when the subducted oceanic crust is thick, but much higher entrainment rate than case 3 after the subducted oceanic crust becomes thinner and more difficult to accumulate in the lowermost mantle. The similar accumulation rate among cases 3-6 may be because they have similar thickness of oceanic crust during the early stages of the model run, which is a major factor that controls the accumulation rate. However, by using lower buoyancy number of oceanic crust in case 4 or smaller activation energy for the temperature-dependence of viscosity in case 5, or by including weak pPv phase in case 6, the PCAs are easier to be stirred into the background mantle by convection flows. These results are consistent with the study of (Christensen and Hofmann, 1994) who showed that the ratio of crustal content in PCAs relative to the total crustal content increases with the buoyancy number of oceanic crust and the degree of temperaturedependence of viscosity, and are consistent with the study of (Li et al., 2014b) who found that weak pPv reduces the stability of thermochemical piles in the lowermost mantle. These results also suggest that by further increasing (decreasing) the buoyancy number of oceanic crust and the degree of temperature-dependence of viscosity would increase (decrease) the amount of crustal segregation and the stability and the overall size of PCAs in the lowermost mantle.

We also found that  $R_n$  decreases with the increase of Rayleigh number by comparing the results of case 7 and case 3 (Fig. 4c), which is consistent with the study of (Christensen and Hofmann, 1994). This may be because by increasing the Rayleigh number, the thickness of oceanic crust that is subducted to the deep mantle becomes thinner and as explained by Christensen and Hofmann (1994), the basal thermal boundary layer (TBL) also becomes thinner which causes less amount of subducted oceanic crust to enter

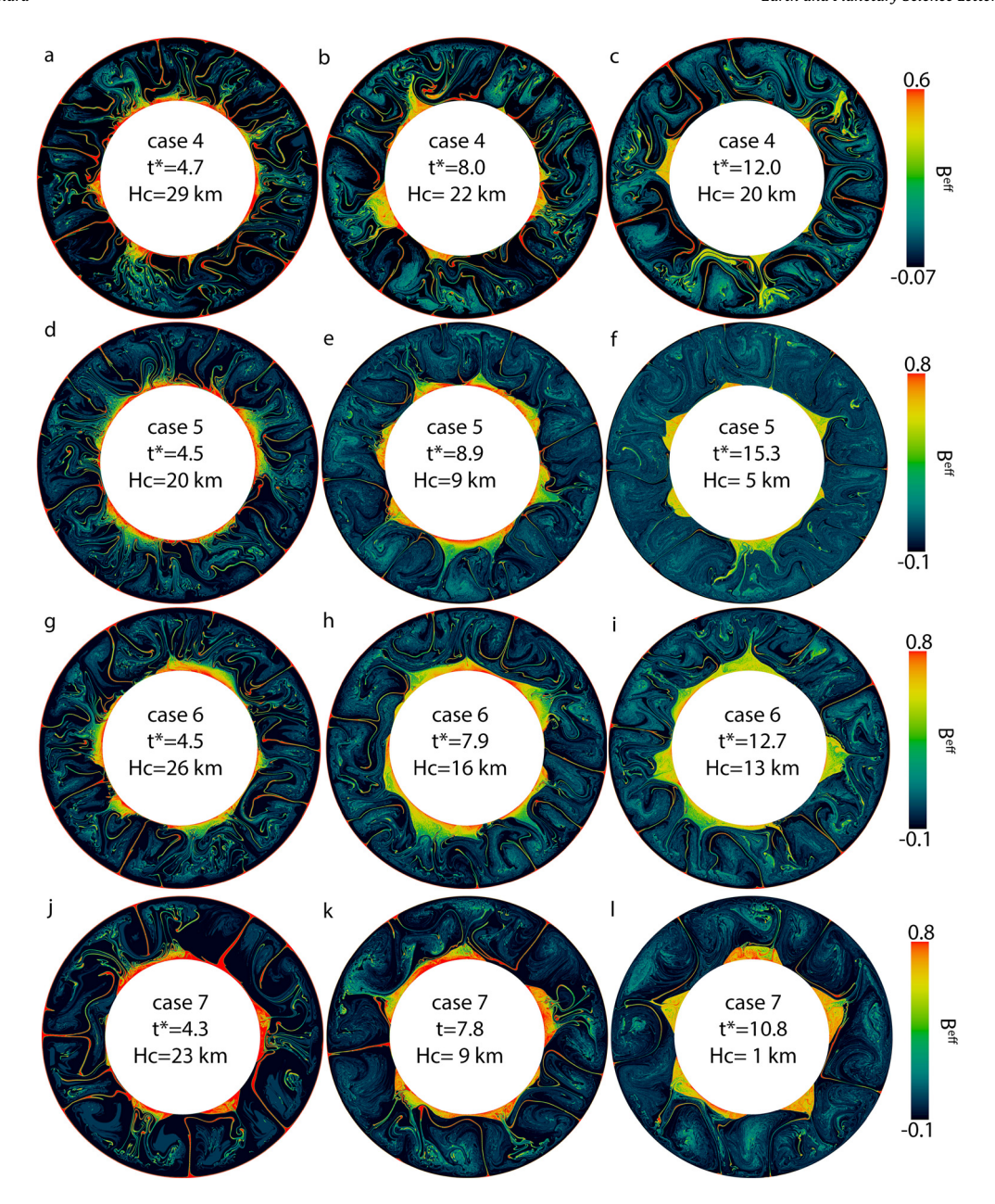


**Fig. 5.** Snapshots of compositional fields (represented by the effective buoyancy ratio) for case 4 (**a-c**), case 5 (**d-f**), case 6 (**g-i**) and case 7 (**j-l**).  $H_c$  and  $t^*$  in each panel are the thickness of oceanic crust and the transit time, respectively.

the basal TBL to segregate. However, it should also be pointed out that other studies have also found the size of crustal accumulations increases with Rayleigh number (e.g., Brandenburg and van Keken, 2007; Nakagawa and Tackley, 2014). The effects of Rayleigh number on the segregation of subducted oceanic crust in the lowermost mantle are discussed in more details in (Li, 2021). Besides its effect on the efficiency of crustal segregation, higher Rayleigh number (which means more vigor of convection) generally leads to faster morphologic change of PCAs when measured by diffusive time scale (Supplementary Information Figure S1). Because the speed of the morphologic change of PCAs is significantly affected by model parameters (e.g., crustal thickness and density, mantle viscosity) that remains not well constrained for the real Earth and because our models are not meant to capture all complexities of the real Earth (e.g., the process of generating plate subduction) that remains not well known, it is difficult to reach a clear-cut conclusion about how much subducted oceanic crust remains in the present-day Earth's lowermost mantle and whether the presentday crustal accumulations, if there is any, have chemically fuzzy or sharp top boundaries.

However, as shown in Figs. 4 and 5, all cases 3-7 show the same trends for the time evolution of the size, the sharpness of top boundaries, and the internal structures of PCAs. These results may remain valid when including additional model complexities if the thickness of oceanic crust is to the first order proportional to uppermost mantle temperature which decreases with time. Firstly, the oceanic crust is likely enriched in heat producing elements (HPEs) than the background mantle, and by including this complexity in our models would increase the temperature and thus buoyancy of PCAs. The effect of adding HPEs to oceanic crust may therefore be like that of choosing a lower buoyancy number for the oceanic crust which, as shown in case 4, does not change the overall trend of the morphologic evolution of PCAs. Secondly, due to larger extent of partial melting beneath mid-ocean ridges. the oceanic crust produced in the early Earth may have more MgO content than that produced at the present-day. However, recently high-temperature-pressure experiments by (Ko et al., 2020) showed that the intrinsic density anomaly of Archean oceanic crust relative to pyrolite at  $> \sim 800$  km depth in the lower mantle is similar to (or only  $\sim$ 0.008 g/cm $^3$  lower than) the intrinsic density anomaly of modern oceanic crust. Therefore, by including a time dependence of composition and density of oceanic crust in our models may not significantly affect our results. Similarly, the thickness and composition of the depleted lithosphere may change with the degree of partial melting. The depleted lithosphere can be viewed as a layer containing a mixture of background mantle materials and intrinsically less dense Harzburgite (e.g., Ringwood and Irifune, 1988). Because the magnitude of the intrinsic density anomaly of Harzburgite is much smaller than that of oceanic crust (e.g., Ringwood and Irifune, 1988) and because most parts of the depleted lithosphere only contains a small portion of Harzburgite (e.g., Ringwood and Irifune, 1988), the average magnitude of the intrinsic density anomaly of the depleted lithosphere is likely much smaller than that of oceanic crust. Therefore, we do not expect adding more complexities to simulate the changes of thickness and buoyancy number of the depleted lithosphere would significantly affect our results. Thirdly, Davies (2008) found that phase transformation at 660 km depth may cause subducted oceanic crust in the early Earth to temporarily accumulate at the base of the transition zone before sinking to the lowermost mantle. This mechanism of 'basalt barrier' may lead to episodic increase of PCA area in the early stages of the calculation but may not alter the overall trend of the morphologic change of PCAs as shown in Figs. 4 and 5.

The evolving morphology of the crustal accumulations in the lowermost mantle provides new understandings on the morphology of the seismically-observed LLSVPs. Seismic observations have suggested that the shear-wave velocity (Vs) of the LLSVPs decreases with depth (e.g., He et al., 2006; Ritsema et al., 2011; Wen, 2001). This negative gradients of  $V_s$  within LLSVPs have been previously proposed to be caused by an increasing degree of partial melting with depth (He et al., 2006; Wen, 2001), or compositional layering of primordial materials and subducted oceanic crust (Ballmer et al., 2016). Here, we show that thermochemical piles formed purely by the accumulations of subducted oceanic crust can also exhibit layered structures, with both the temperature anomaly (with respect to the surrounding mantle) and the intrinsic density of the piles increase with depth (Figs. 2a, b), which may explain the decrease of  $V_s$  with depth within the LLSVPs. Similar conclusion has been reached recently by (Jones et al., 2020) who converted the temperature and compositional fields in the models of (Brandenburg et al., 2008) into seismic velocities which they found are comparable to that of the LLSVPs in the tomography model of S40RTS (Ritsema et al., 2011). One caveat found in our study is that the interiors of PCAs can gradually become more homogeneous, and it remains difficult to conclude whether the depth dependence of  $V_s$  of the present-day LLSVPs can be solely explained by the accumulation of subducted oceanic crust.

Sharp tops of the LLSVPs have been reported locally, e.g., at the western edges of the Africa LLSVP (Sun and Miller, 2013) and the northern edges of the Pacific LLSVP (Zhao et al., 2015). We show that some crustal accumulations may gain sharp top boundaries sooner than others (Fig. 5), indicating that it is not unlikely that other regions of the LLSVPs may have more fuzzy top boundaries. To confirm this possibility requires further seismic observations at other regions of the LLSVPs. Nevertheless, if the LLSVPs were later found to have sharp top boundaries everywhere, it does not exclude the possibility that the LLSVPs are caused by the accumulation of subducted oceanic crust. In such case, the majority of the LLSVPs may be produced in the early Earth when the mantle may be hotter, and the oceanic crust was much thicker than present-day, and they may have gradually gained sharp tops through time.

Geochemical observations have shown recycled oceanic crust with ages ranging from Archean time (Cabral et al., 2013) to geologically recent (Sobolev et al., 2011) in the sources of OIBs. Our results suggest that crustal accumulations may be dominated by relatively old subducted oceanic crust (e.g., Fig. 4). Whereas relatively old crustal materials can be entrained into mantle plumes from these crustal accumulations, young subducted oceanic crust is more likely to be directly entrained up by mantle plumes without accumulating in the lowermost mantle (e.g., Li, 2021; Li et al., 2014a). The entrainment of subducted oceanic crust with variable ages by mantle plumes to the uppermost mantle may explain the vastly different ages of recycled oceanic crust in the OIB sources.

#### 5. Conclusion

Here, we perform thermochemical geodynamic calculations to study the morphological evolution of accumulations of subducted oceanic crust in the lowermost mantle. In our models, the oceanic crust thins with the cooling of uppermost mantle. We find that the size of the crustal accumulations first increases with time when the oceanic crust is thick. However, materials from the crustal accumulations are entrained into the surrounding mantle throughout the model run. As mantle cools and the oceanic crust becomes thinner, the subducted oceanic crust becomes more difficult to accumulate on the CMB; consequently, the size of the crustal accumulations decreases. In addition, the crustal accumulations often start with chemically fuzzy top boundaries and stratified interiors when the oceanic crust is thick, and then gradually gain sharp boundaries and more homogeneous internal structures as oceanic crust thins. If the LLSVPs are mainly caused by the accumulations of subducted oceanic crust, most parts of them may be produced in the early Earth when the mantle was hotter, and the oceanic crust was thicker. They may start with chemically fuzzy top boundaries and stratified interiors and gradually develop into sharper top boundaries and more homogeneous interiors.

#### **CRediT authorship contribution statement**

**Mingming Li:** Conceptualization, Investigation, Methodology, Visualization, Writing – original draft. **Allen K. McNamara:** Conceptualization, Methodology, Writing – original draft.

#### **Declaration of competing interest**

The authors declare that they have no known competing financial interests or personal relationships that could have appeared to influence the work reported in this paper.

#### Acknowledgements

M. Li is supported by NSF grants EAR-1849949 and EAR-1855624. A. McNamara is supported by NSF grants EAR-1722623 and EAR-1664332. We thank Paul Tackley and two anonymous reviewers for their constructive comments. Geodynamic models were performed on the Agave cluster at Arizona State University. There is no conflict of interest.

#### Appendix A. Supplementary material

Supplementary material related to this article can be found online at https://doi.org/10.1016/j.epsl.2021.117265.

#### References

Ammann, M.W., Brodholt, J.P., Wookey, J., Dobson, D.P., 2010. First-principles constraints on diffusion in lower-mantle minerals and a weak D" layer. Nature 465, 462–465. https://doi.org/10.1038/nature09052.

- Ballmer, M.D., Schumacher, L., Lekic, V., Thomas, C., Ito, G., 2016. Compositional layering within the large low shear-wave velocity provinces in the lower mantle. Geochem. Geophys. Geosyst. 17, 5056–5077. https://doi.org/10.1002/ 2016gc006605.
- Brandenburg, J.P., Hauri, E.H., van Keken, P.E., Ballentine, C.J., 2008. A multiplesystem study of the geochemical evolution of the mantle with force-balanced plates and thermochemical effects. Earth Planet. Sci. Lett. 276, 1–13. https:// doi.org/10.1016/j.epsl.2008.08.027.
- Brandenburg, J.P., van Keken, P.E., 2007. Deep storage of oceanic crust in a vigorously convecting mantle. J. Geophys. Res. 112, B06403. https://doi.org/10.1029/2006jb004813.
- Cabral, R.A., Jackson, M.G., Rose-Koga, E.F., Koga, K.T., Whitehouse, M.J., Antonelli, M.A., Farquhar, J., Day, J.M., Hauri, E.H., 2013. Anomalous sulphur isotopes in plume lavas reveal deep mantle storage of Archaean crust. Nature 496, 490–493. https://doi.org/10.1038/nature12020.
- Christensen, U.R., Hofmann, A.W., 1994. Segregation of subducted oceanic crust in the convecting mantle. J. Geophys. Res. 99, 19867–19884. https://doi.org/10. 1029/93/B03403.
- Davies, G.F., 2008. Episodic layering of the early mantle by the 'basalt barrier' mechanism. Earth Planet. Sci. Lett. 275, 382–392. https://doi.org/10.1016/j.epsl.2008.08.036.
- Deschamps, F., Cobden, L., Tackley, P.J., 2012. The primitive nature of large low shear-wave velocity provinces. Earth Planet. Sci. Lett. 349, 198–208. https:// doi.org/10.1016/j.epsl.2012.07.012.
- Garnero, E.J., McNamara, A.K., Shim, S.-H., 2016. Continent-sized anomalous zones with low seismic velocity at the base of Earth's mantle. Nat. Geosci. 9, 481–489. https://doi.org/10.1038/ngeo2733.
- He, Y.M., Wen, L.X., Zheng, T.Y., 2006. Geographic boundary and shear wave velocity structure of the "Pacific anomaly" near the core-mantle boundary beneath western Pacific. Earth Planet. Sci. Lett. 244, 302–314. https://doi.org/10.1016/j.epsl.2006.02.007.
- Hernlund, J.W., Tackley, P.J., 2008. Modeling mantle convection in the spherical annulus. Phys. Earth Planet. Inter. 171, 48–54. https://doi.org/10.1016/j.pepi.2008.
- Hirose, K., Takafuji, N., Sata, N., Ohishi, Y., 2005. Phase transition and density of subducted MORB crust in the lower mantle. Earth Planet. Sci. Lett. 237, 239–251. https://doi.org/10.1016/j.epsl.2005.06.035.
- Hofmann, A.W., 1997. Mantle geochemistry: the message from oceanic volcanism. Nature 385, 219–229. https://doi.org/10.1038/385219a0.
- Hunt, S.A., Weidner, D.J., Li, L., Wang, L.P., Walte, N.P., Brodholt, J.P., Dobson, D.P., 2009. Weakening of calcium iridate during its transformation from perovskite to post-perovskite. Nat. Geosci. 2, 794–797. https://doi.org/10.1038/Ngeo663.
- Jones, T.D., Maguire, R.R., van Keken, P.E., Ritsema, J., Koelemeijer, P., 2020. Subducted oceanic crust as the origin of seismically slow lower-mantle structures. Prog. Earth Planet. Sci. 7, 17. https://doi.org/10.1186/s40645-020-00327-1.
- Kesson, S.E., Fitz Gerald, J.D., Shelley, J.M.G., 1994. Mineral chemistry and density subducted basaltic crust at lower-mantle pressures. Nature 372, 767–769. https://doi.org/10.1038/372767a0.
- Ko, B., Prakapenka, V., Kunz, M., Prescher, C., Leinenweber, K., Shim, S.-H., 2020. Mineralogy and density of Archean volcanic crust in the mantle transition zone. Phys. Earth Planet. Inter. 305, 106490. https://doi.org/10.1016/j.pepi.2020. 106490.
- Koelemeijer, P., Deuss, A., Ritsema, J., 2017. Density structure of Earth's lowermost mantle from Stoneley mode splitting observations. Nat. Commun. 8, 15241. https://doi.org/10.1038/ncomms15241.
- Langmuir, C.H., Klein, E.M., Plank, T., 1992. Petrological systematics of mid-ocean ridge basalts: constraints on melt generation beneath ocean ridges. In: Morgan, Phipps, Blackman, Sinton (Eds.), Mantle Flow and Melt Generation at Mid-Ocean Ridges. In: Geophysical Monograph, vol. 71. American Geophysical Union, pp. 183–280.
- Lau, H.C.P., Mitrovica, J.X., Davis, J.L., Tromp, J., Yang, H.Y., Al-Attar, D., 2017. Tidal tomography constrains Earth's deep-mantle buoyancy. Nature 551, 321–326. https://doi.org/10.1038/nature24452.
- Li, M., 2021. The cycling of subducted oceanic crust in the Earth's deep mantle. In: Mantle Convection and Surface Expressions. In: Geophysical Monograph Series, pp. 303–328. https://doi.org/10.1002/9781119528609.ch12.
- Li, M., Black, B., Zhong, S., Manga, M., Rudolph, M.L., Olson, P., 2016. Quantifying melt production and degassing rate at mid-ocean ridges from global mantle convection models with plate motion history. Geochem. Geophys. Geosyst. 17, 2884–2904. https://doi.org/10.1002/2016gc006439.
- Li, M., McNamara, A.K., 2013. The difficulty for subducted oceanic crust to accumulate at the Earth's core-mantle boundary. J. Geophys. Res. 118, 1807–1816. https://doi.org/10.1002/Jgrb.50156.
- Li, M., McNamara, A.K., 2018. The influence of deep mantle compositional heterogeneity on Earth's thermal evolution. Earth Planet. Sci. Lett. 500, 86–96. https://doi.org/10.1016/j.epsl.2018.08.009.
- Li, M., McNamara, A.K., Garnero, E.J., 2014a. Chemical complexity of hotspots caused by cycling oceanic crust through mantle reservoirs. Nat. Geosci. 7, 366–370. https://doi.org/10.1038/Ngeo2120.

- Li, M., McNamara, A.K., Garnero, E.J., Yu, S., 2017. Compositionally-distinct ultra-low velocity zones on Earth's core-mantle boundary. Nat. Commun. 8, 177. https:// doi.org/10.1038/s41467-017-00219-x.
- Li, M., Zhong, S.J., 2017. The source location of mantle plumes from 3D spherical models of mantle convection. Earth Planet. Sci. Lett. 478, 47–57. https://doi.org/ 10.1016/j.epsl.2017.08.033.
- Li, M., Zhong, S.J., Olson, P., 2018. Linking lowermost mantle structure, core-mantle boundary heat flux and mantle plume formation. Phys. Earth Planet. Inter. 277, 10–29. https://doi.org/10.1016/j.pepi.2018.01.010.
- Li, Y., Deschamps, F., Tackley, P.J., 2014b. Effects of low-viscosity post-perovskite on the stability and structure of primordial reservoirs in the lower mantle. Geophys. Res. Lett. 41, 7089–7097. https://doi.org/10.1002/2014GL061362.
- McKenzie, D., Bickle, M.J., 1988. The volume and composition of melt generated by extension of the lithosphere. J. Petrol. 29, 625–679. https://doi.org/10.1093/petrology/29.3.625.
- Mulyukova, E., Steinberger, B., Dabrowski, M., Sobolev, S.V., 2015. Survival of LLSVPs for billions of years in a vigorously convecting mantle: replenishment and destruction of chemical anomaly. J. Geophys. Res., Solid Earth 120, 3824–3847. https://doi.org/10.1002/2014jb011688.
- Nakagawa, T., Tackley, P.J., 2005. Deep mantle heat flow and thermal evolution of the Earth's core in thermochemical multiphase models of mantle convection. Geochem. Geophys. Geosyst. 6, Q08003. https://doi.org/10.1029/2005gc000967.
- Nakagawa, T., Tackley, P.J., 2010. Influence of initial CMB temperature and other parameters on the thermal evolution of Earth's core resulting from thermochemical spherical mantle convection. Geochem. Geophys. Geosyst. 11, Q06001. https://doi.org/10.1029/2010gc003031.
- Nakagawa, T., Tackley, P.J., 2014. Influence of combined primordial layering and recycled MORB on the coupled thermal evolution of Earth's mantle and core. Geochem. Geophys. Geosyst. 15, 619–633. https://doi.org/10.1002/2013GC005128.
- Nakagawa, T., Tackley, P.J., 2015. Influence of plate tectonic mode on the coupled thermochemical evolution of Earth's mantle and core. Geochem. Geophys. Geosyst. 3400 (3413). https://doi.org/10.1002/2015GC005996.
- Nakagawa, T., Tackley, P.J., Deschamps, F., Connolly, J.A.D., 2010. The influence of MORB and harzburgite composition on thermo-chemical mantle convection in a 3-D spherical shell with self-consistently calculated mineral physics. Earth Planet. Sci. Lett. 296, 403–412. https://doi.org/10.1016/j.epsl.2010.05.026.
- O'Farrell, K.A., Lowman, J.P., 2010. Emulating the thermal structure of spherical shell convection in plane-layer geometry mantle convection models. Phys. Earth Planet. Inter. 182, 73–84. https://doi.org/10.1016/j.pepi.2010.06.010.
- Ogawa, M., 2003. Chemical stratification in a two-dimensional convecting mantle with magmatism and moving plates. J. Geophys. Res., Solid Earth 108, 2561. https://doi.org/10.1029/2002jb002205.
- Ringwood, A.E., Irifune, T., 1988. Nature of the 650-km seismic discontinuity: implications for mantle dynamics and differentiation. Nature 331, 131–136. https://doi.org/10.1038/331131a0.
- Ritsema, J., Deuss, A., van Heijst, H.J., Woodhouse, J.H., 2011. S40RTS: a degree-40 shear-velocity model for the mantle from new Rayleigh wave dispersion, teleseismic traveltime and normal-mode splitting function measurements. Geophys. J. Int. 184, 1223–1236. https://doi.org/10.1111/j.1365-246X.2010.04884.x.
- Sobolev, A.V., Hofmann, A.W., Jochum, K.P., Kuzmin, D.V., Stoll, B., 2011. A young source for the Hawaiian plume. Nature 476, 434–437. https://doi.org/10.1038/nature10321.
- Sun, D., Miller, M.S., 2013. Study of the western edge of the African large low shear velocity province. Geochem. Geophys. Geosyst. 14, 3109–3125. https://doi.org/10.1002/ggge.20185.
- Tackley, P.J., King, S.D., 2003. Testing the tracer ratio method for modeling active compositional fields in mantle convection simulations. Geochem. Geophys. Geosyst. 4, 8302. https://doi.org/10.1029/2001gc000214.
- Thomson, A.R., Crichton, W.A., Brodholt, J.P., Wood, I.G., Siersch, N.C., Muir, J.M.R., Dobson, D.P., Hunt, S.A., 2019. Seismic velocities of CaSiO3 perovskite can explain LLSVPs in Earth's lower mantle. Nature 572, 643–647. https://doi.org/10.1038/s41586-019-1483-x.
- Torsvik, T.H., Burke, K., Steinberger, B., Webb, S.J., Ashwal, L.D., 2010. Diamonds sampled by plumes from the core-mantle boundary. Nature 466, 352–355. https://doi.org/10.1038/nature09216.
- Trim, S.J., Heron, P.J., Stein, C., Lowman, J.P., 2014. The feedback between surface mobility and mantle compositional heterogeneity: implications for the Earth and other terrestrial planets. Earth Planet. Sci. Lett. 405, 1–14. https://doi.org/10.1016/j.epsl.2014.08.019.
- Wang, W., Xu, Y., Sun, D., Ni, S., Wentzcovitch, R., Wu, Z., 2020. Velocity and density characteristics of subducted oceanic crust and the origin of lower-mantle heterogeneities. Nat. Commun. 11, 64. https://doi.org/10.1038/s41467-019-13720-2.
- Wen, L.X., 2001. Seismic evidence for a rapidly varying compositional anomaly at the base of the Earth's mantle beneath the Indian Ocean. Earth Planet. Sci. Lett. 194, 83–95. https://doi.org/10.1016/S0012-821x(01)00550-7.

Zhao, C., Garnero, E.J., McNamara, A.K., Schmerr, N., Carlson, R.W., 2015. Seismic evidence for a chemically distinct thermochemical reservoir in Earth's deep mantle beneath Hawaii. Earth Planet. Sci. Lett. 426, 143–153. https://doi.org/10.1016/j.epsl.2015.06.012.

Zhong, S., 2006. Constraints on thermochemical convection of the mantle from plume heat flux, plume excess temperature, and upper mantle temperature. J. Geophys. Res. 111, B04409. https://doi.org/10.1029/2005jb003972.